Scattering-assisted tunneling: Energy dependence, magnetic field dependence, and use as an external probe of two-dimensional transport

K. J. Russell, F. Capasso, and V. Narayanamurti[*]

School of Engineering and Applied Sciences, Harvard University, Cambridge, Massachusetts 02138, USA

H. Lu, J. M. O. Zide,[†] and A. C. Gossard

Materials Department, University of California, Santa Barbara, California 93106, USA

For more than three decades, research on tunneling through planar barriers has focused principally on processes that conserve momentum parallel to the barrier. Here we investigate transport in which scattering destroys lateral momentum conservation and greatly enhances the tunneling probability. We have measured its energy dependence using capacitance spectroscopy, and we show that for electrons confined in a quantum well, the scattering enhancement can be quenched in an applied magnetic field, enabling this mechanism to function as an external probe of the origin of the quantum Hall effect.

I. INTRODUCTION

The tendency in semiconductor science and technology has been to strive for materials with greatly reduced defect density. This has resulted in tunneling devices such as resonant tunneling diodes (RTDs) (Ref. 1) and quantum cascade (QC) lasers[2] that require nearly ideal translational invariance in the plane of the layers to impose lateral momentum conservation and restrict transport to quantum resonances. There are times, however, when defects are necessary to observe new effects. A notable example of this is the integer quantum Hall effect[3] in which defects provide the energy states that allow the chemical potential to lie between Landau levels—a necessary condition for observing the effect. Nevertheless, the possible utility of nonideal planar tunneling has been largely overlooked. Experimental results have suggested[4–8] and theory has shown[9–11] that under certain conditions tunneling through planar barriers can be fundamentally altered by electron scattering. Here we use capacitance-voltage spectroscopy to measure the energy dependence of this scattering-assisted tunneling and show that the enhancement due to scattering can be quenched in a magnetic field. By enabling simultaneous measurements of the thermodynamic density of states (TDOS) and the transport characteristics of a two-dimensional electron gas (2DEG), this measurement offers a way to probe the origin of the zero-resistance states of the integer quantum Hall effect using only transport orthogonal to the plane of the 2DEG.

This paper is organized as follows. In Sec. II we present our method of measuring the quasibound state lifetime and show how this measurement can be used to probe the energy dependence of electron tunneling. Section III details the sample structure used in our measurements as well as general constraints on the design of samples dominated by scattering-assisted tunneling. In Secs. IV and V, we present experimental results of the energy dependence and magnetic field dependence, respectively, of scattering-assisted tunneling. Finally, in Sec. VI we discuss possible uses and implications for scattering-assisted tunneling.

II. MEASURING QUASIBOUND STATE LIFETIME

Our goal is to measure the effects of momentum conservation and nonconservation on tunneling in planar semiconductor heterostructures. Although the tunneling mechanisms we are investigating are also relevant to general tunneling between three-dimensional (3D) contacts, the effect of momentum conservation becomes more apparent when one of the contacts is a 2DEG. This is because the quantum confinement that defines the 2DEG only allows the momentum perpendicular to the interfaces to have certain, discrete values. Within each of these 2DEG subbands, different electron states differ only in their parallel momentum, so monitoring the tunneling rate while varying the occupation of a subband can provide a direct measurement of the degree of parallel momentum conservation.

The rate ν_T at which electrons escape from a 2DEG by tunneling is proportional to the tunneling probability T, and the inverse of ν_T defines the quasibound state lifetime τ_ℓ. Using the WKB approximation, valid for barriers of small transparency, the tunneling probability in the absence of scattering can be calculated as

$$T_0 \approx \exp(-2\ell\sqrt{2m(\phi-\varepsilon_0)}/\hbar), \qquad (1)$$

where m is the electron effective mass, ε_0 is the 2DEG ground-state energy, ϕ is the height of the energy barrier, ℓ is its thickness, and $\hbar = h/2\pi$ is Planck's constant. Note that ε_0 is the only relevant energy scale. Neither the (in-plane) kinetic energy ε_K nor the total energy $\varepsilon = \varepsilon_0 + \varepsilon_K$ enter in the description of the tunneling process; in the absence of scattering T is independent of ε_K. This is a consequence of translational invariance and conservation of the component of momentum parallel to the tunnel barrier (TB), $\hbar k_\parallel = \sqrt{2m\varepsilon_K}$. Such invariance is an excellent approximation because the correlation length of interface roughness in state-of-the-art heterojunctions is small compared to the inverse Fermi wave vector $k_F^{-1} = (2\pi n_S)^{-1/2}$, where n_S is the 2DEG carrier density.[12]
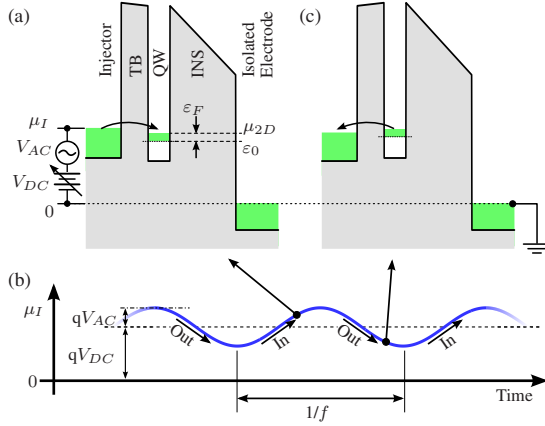
FIG. 1. (Color online) (a) Schematic conduction-band diagram of a typical heterostructure used in our investigation, shown as the chemical potential μ_I of the injector is increasing so that electrons are tunneling through the TB into vacant 2DEG states in the QW. The insulating barrier (INS) is opaque to tunneling at the values of V_{dc} used in this experiment. (b) Evolution of μ_I over time for V_{ac} of frequency f. If τ_ℓ is much longer than the period $1/f$, then the 2DEG cannot charge or discharge fast enough for μ_{2D} to follow μ_I, and the device capacitance (measured between the injector and isolated electrode) will decrease. (c) as in (a) but shown with V_{ac} advanced 1/2 cycle so that electrons are tunneling out of the 2DEG into the injector.

In the opposite regime, $k_\parallel$ is not conserved[13] but is instead coupled into perpendicular tunneling by scattering. This enhances the tunneling probability by redirecting the electron toward the tunnel barrier, effectively reducing the barrier height by a fraction of the kinetic energy ε_K. Meshkov[9] showed theoretically that the barrier height reduction reaches the full value of ε_K in the limit of a very thick barrier. In such a scenario, the tunneling probability T_ε depends on the total energy ε rather than on ε_0 alone and is proportional to

$$\exp(-2\ell\sqrt{2m(\phi - \varepsilon_0 - \varepsilon_K)}/\hbar). \qquad (2)$$

The explicit dependence on ε_K makes this tunneling mechanism a sensitive function of transport within the 2DEG.

In our samples, tunneling occurs between the ground state of a 2DEG and a 3D contact. [See Fig. 1(a) for example sample structure.] Tunneling into 2DEGs is responsible for the characteristic dc transport resonances of RTDs and QC lasers; however, dc measurements are not well suited to characterizing this tunneling, especially the energy dependence. This is because there is no low-resistance path for electrons to exit the 2DEG once they tunnel into it. The exit path therefore forms a resistive divider with the tunnel barrier, and the voltage drop across the tunnel barrier is thus not accurately known. A similar problem occurs when measuring the capacitance of metal-oxide-semiconductor field-effect transistors at high values of perpendicular magnetic field,[14–16] and this difficulty has necessitated sophisticated capacitive techniques to measure such basic quantities as the density of states of 2DEGs.[17]

We therefore design the insulating (INS) barrier in our samples to block dc transport over the range of dc biases V_{dc}
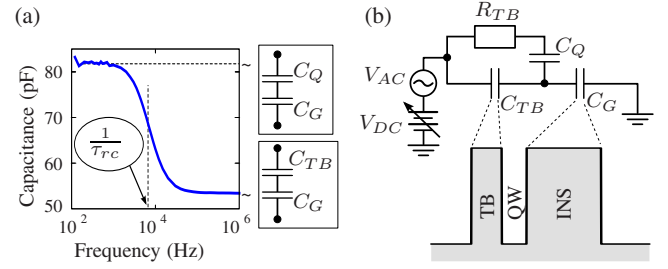

FIG. 2. (Color online) (a) Representative capacitance-frequency curve from an impedance measurement on sample N. (b) Device equivalent circuit that we use to fit measured impedance traces, thereby allowing us to determine τ_{rc}. Fits are made simultaneously to both the active and reactive impedance components. C_Q is the capacitance of the 2DEG and $R_{TB} = \tau_{rc}/C_Q$ is the tunneling resistance of the TB, yielding an RC time constant of τ_{rc}. C_{TB} and C_G are geometric capacitances of the TB and INS barrier, respectively.

used in the experiment. Because the insulating barrier is opaque to tunneling, the chemical potential μ_{2D} of the 2DEG is able to come into equilibrium with the chemical potential μ_I of the 3D injector layer (assuming only a dc bias is applied). V_{dc} can then be used to control the 2DEG Fermi energy ε_F and carrier density n_S, which we calibrate using comparison of simulated and measured capacitance-voltage data, as well as magnetocapacitance measurements.[16,17]

We probe tunneling in and out of the 2DEG in our samples using the complex, frequency-dependent impedance of the device. This technique has been used previously to study energy gaps[18–20] and density of states[21] in 2DEG systems, as well as tunneling times and density of states in buried GaAs (Ref. 22) and InAs (Ref. 23 and 24) quantum dots. We measure the impedance using a sinusoidal ac bias V_{ac} of frequency f, as shown in Fig. 1. The amplitude of V_{ac} is kept small (typically 5 mV$_{rms}$) to cause negligible change in n_S. V_{ac} drives the 2DEG out of quasiequilibrium from the injector to establish a small chemical potential difference $\Delta\mu = \mu_I - \mu_{2D}$ that oscillates with frequency f and causes electrons to tunnel back and forth between injector and 2DEG. However, the number of electrons that tunnel before $\Delta\mu$ reverses sign is limited by the tunneling rate ν_T. This results in two frequency regimes of our device: one for $f \ll \nu_T$ in which electrons have time to tunnel in and out of the 2DEG to follow V_{ac}, and another for $f \gg \nu_T$ in which they do not. At low $f (f \ll \nu_T)$, electrons in the QW are therefore in approximate quasiequilibrium with those in the injector, and $\Delta\mu$ is negligible. V_{ac} is then effectively applied only across the insulating barrier, and the capacitance is at its highest. At high f, quasiequilibrium cannot be maintained and V_{ac} falls across the series combination of the tunnel and insulating barriers, thus lowering the device capacitance as shown in Fig. 2(a).

Each impedance-versus-frequency sweep is fitted using the equivalent circuit shown in Fig. 2(b). This equivalent circuit is derived from balance of charge within the device, as detailed in Appendix A. Our fitting procedure is discussed in Appendix B. Within this equivalent circuit model, the frequency dependence is a result of the series combination of C_Q and R_{TB}, yielding a time constant of $\tau_{rc} = C_Q R_{TB}$. We will

discuss the relation between τ_ℓ and τ_{rc} shortly. R_{TB} represents the resistance associated with tunneling through the tunnel barrier. C_Q is the capacitance of the 2DEG—also known as the inversion layer capacitance[25] or the quantum capacitance—and is equal to $q^2 g_{2D} A$, where q is the electron charge, g_{2D} is the 2DEG TDOS, and A is the device area.[26] By fitting an impedance-frequency sweep using the equivalent circuit shown in Fig. 2(b), we can therefore extract both τ_{rc} and g_{2D} simultaneously.

To provide insight into the physical meaning of the fitting parameters of our equivalent circuit, especially τ_{rc}, it is worth noting the differences between the analysis used here (based on Refs. 23 and 24) and the equivalent but distinct approach used by Ashoori *et al.*[18,19,21] Ashoori *et al.* fit their data to a different equivalent circuit than ours, with the goal of determining the tunneling conductance $G_{TB} = q^2 g_s A / \tau_\ell$, where g_s is the single-particle density of states. In their case, they assume τ_ℓ to be constant and all variations in G_{TB} are attributed to g_s. (As we will show later, this assumption is justified for their sample design.) In our case, we are interested in variations in τ_ℓ, but we actually measure τ_{rc}. As is detailed in Appendix A, τ_ℓ and τ_{rc} are related by

$$\tau_{rc} = \frac{g_{2D}}{g_s} \tau_\ell. \tag{3}$$

As shown by Ashoori *et al.*, in an applied magnetic field $g_{2D} = g_s$ is not generally true, and in Sec. V we will discuss how the relative Landau-level filling-factor dependence of g_s and g_{2D} nevertheless allow us to qualitatively determine the behavior of τ_ℓ.

It is also worth noting that Eq. (3) allows us to easily obtain the tunneling conductance of Ref. 18,

$$G_{TB} = \frac{q^2 g_{2D} A}{\tau_{rc}} = \frac{C_Q}{\tau_{rc}} = R_{TB}^{-1}. \tag{4}$$

The results from this method of determining G_{TB} agree with the results obtained using the analysis of Ashoori *et al.*, as is also shown in Appendix A. For our purposes, however, τ_{rc} is a more useful quantity than G_{TB}. This is because our goal is to observe changes in τ_ℓ independent of changes in g_s, and the inclusion of g_{2D}, which varies with Landau-level filling factor in a way similar to g_s, partially cancels variations in g_s in Eq. (3). This makes τ_{rc} a less sensitive function of g_s and thus a more accurate approximation to τ_ℓ.

III. TUNNEL BARRIER DESIGN

As Meshkov showed with a rigorous calculation,[9] the tunnel barrier morphology is the aspect of the sample that most directly affects whether or not scattering-assisted tunneling will dominate. Using a less rigorous but more conceptually simple approach, we can illustrate the essential physics that determines the characteristics of transport and can design samples to operate in each transport regime.

In terms of the WKB formulation of Eqs. (1) and (2), scattering enables the kinetic energy associated with motion parallel to the QW to be coupled into transport in the perpendicular direction, thereby increasing the probability that
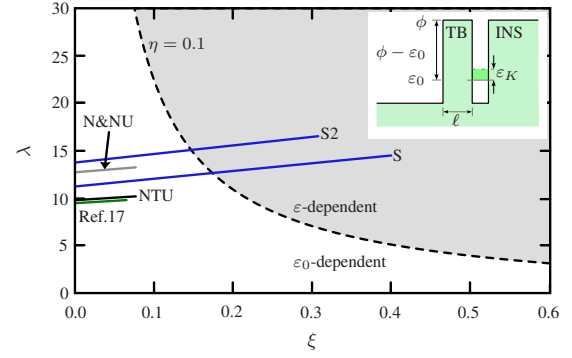

FIG. 3. (Color online) Diagram depicting the energy dependence of the tunneling as a function of scaled barrier thickness $\lambda = \ell / \ell_0$ and scaled electron kinetic energy $\xi = \varepsilon_K / (\phi - \varepsilon_0)$. For small λ and ξ (i.e., the lower left, unshaded area of the diagram), transport is predominantly momentum conserving and is approximately described by Eq. (1). In the opposite regime (shaded region), transport is dominated by scattering-assisted tunneling and varies with ε, as in Eq. (2). Using Eq. (8) and the scaled scattering rate η, one can find values of ξ and λ for which the two transport mechanisms yield approximately the same tunneling rate (broken line, calculated for $\eta = 0.1$, corresponding to an approximate sheet mobility of 5×10^4 cm^2 V^{-1} s^{-1} for an InGaAs QW with a 30 meV ground-state confinement energy). The overlaid lines indicate the approximate regimes of operation of several different samples over a range of ε_K; only samples S and S2 extend into the scattering-assisted tunneling regime. Inset: partial schematic band diagram of a sample showing parameter definitions.

an electron will escape from the quasibound state of a quantum well (QW). However, if the kinetic energy ε_K is small compared to the barrier height ϕ, this increase will be negligible. And even if the increase is significant, it requires the electron to scatter, which may not occur with sufficient frequency to affect the transport. The interplay between these factors can be captured in a diagram, shown in Fig. 3, that delineates between types of tunneling transport. To construct the diagram, we consider tunneling through the idealized square barrier shown in the inset of Fig. 3.

The tunneling rate in the case of momentum-conserved tunneling is simply $\nu_0 T_0$, where $\nu_0 = \varepsilon_0 / h$ is the tunnel-attempt frequency of an electron in the bound state and T_0 is the tunneling probability calculated according to Eq. (1).[27] In the case of scattering-assisted tunneling, the relevant tunneling-attempt frequency is ν_S, the scattering rate, so the tunneling rate is given by $\nu_S T_\varepsilon$, where T_ε is the tunneling probability of a scattered electron given by Eq. (2). The transport through the barrier will therefore be dominated by scattering-assisted tunneling when the following inequality holds:

$$\frac{T_\varepsilon}{T_0} \gg \frac{1}{\eta}, \tag{5}$$

where $\eta = \nu_S / \nu_0$ can be thought of as a nondimensional scattering rate. We wish to determine the values of barrier height and thickness for which Eq. (5) is valid. Using Eqs. (1) and (2), we find

TABLE I. Comparison between samples highlighting the InAlAs/InGaAs alloy fraction of the tunnel barrier (X), the conduction-band offset of the tunnel barrier (ΔE_C), the thickness of the tunnel barrier (ℓ), the level of Si δ doping within the quantum well (δ) as estimated by capacitance-voltage and magnetocapacitance measurements, and the thickness w of the undoped layer adjacent to the tunnel barrier.

Sample	X	ΔE_C (eV)	ℓ (nm)	δ (10^{11} cm^{-2})	w (nm)
NTU	1.0	0.52	10	0	5
NU	1.0	0.52	13	0	5
N	1.0	0.52	13	1.5	5
S	0.2	0.10	40	2	10
S2	0.25	0.13	40	2	10

$$\frac{1}{2}\log\left(\frac{1}{\eta}\right) \ll \ell \frac{\sqrt{2m(\phi-\varepsilon_0)}}{\hbar}\left(1-\sqrt{1-\frac{\varepsilon_K}{\phi-\varepsilon_0}}\right). \quad (6)$$

We can now nondimensionalize this equation to allow easier comparison between systems. We scale the thickness ℓ of the barrier by the characteristic decay length in the barrier $\ell_0 = \hbar/\sqrt{2m(\phi-\varepsilon_0)}$, yielding $\lambda \equiv \ell/\ell_0$. We also scale the kinetic energy ε_K by the effective barrier height, $\phi-\varepsilon_0$, giving $\xi \equiv \varepsilon_K/(\phi-\varepsilon_0)$. Using these definitions, Eq. (6) can be rewritten as

$$\frac{1}{2}\log\left(\frac{1}{\eta}\right) \ll \lambda(1-\sqrt{1-\xi}), \quad (7)$$

which can easily be solved for λ,

$$\lambda \gg \frac{1}{1-\sqrt{1-\xi}}\log\sqrt{\frac{1}{\eta}}. \quad (8)$$

For an electron with scaled kinetic energy ξ undergoing scattering with a scaled scattering rate η, this equation can be used to estimate of the minimum scaled barrier thickness λ that is necessary for the transport to be dominated by scattering-assisted tunneling.

Overlaid on the diagram of Fig. 3 are the estimated transport characteristics of several different tunnel barrier designs. As an initial check, we confirm that the tunneling through the barrier of Ref. 17 is dominated by momentum-conserved tunneling, as was seen experimentally. In the diagram, the expected transport of this sample remains fully within the regime of momentum-conserved transport for the entire experimental range of ε_K. In reality, the sample of Ref. 17 is expected to have a scattering rate η that is orders of magnitude lower than what is plotted in Fig. 3, so it is even less likely that scattering-assisted transport would be observed in that sample than is suggested by our diagram.

The other samples shown in Fig. 3 were designed using the diagram, and the transport properties of these devices are the focus of this report. Of the relevant characteristics, the primary difference between samples was the thickness and alloy content of the tunnel barrier; these differences, as well as those of two other relevant characteristics, are summarized in Table I. Schematic band diagrams of the samples are shown in Fig. 4.

Three samples (N, NU, and NTU) have been designed to exhibit momentum-conserved tunneling. As in the sample from Ref. 17, the barriers in these samples are relatively tall and thin, making $\varepsilon_K/(\phi-\varepsilon_0)$ small for the range of ε_K we can access experimentally ($\varepsilon_K \lesssim 30$ meV). Therefore, as can be seen in Fig. 3, we expect these samples to exhibit momentum-conserved tunneling.

In contrast, the two samples (S and S2) designed to show transport dominated by scattering-assisted tunneling have relatively short, thick tunnel barriers. This makes the experimentally accessible values of ε_K a significant fraction of the effective barrier height $\phi-\varepsilon_0$, leading to a much larger enhancement of the tunneling probability for scattered electrons at high ε_K. As a result, the transport characteristics of these two samples cross into the regime of scattering-assisted tunneling in Fig. 3.
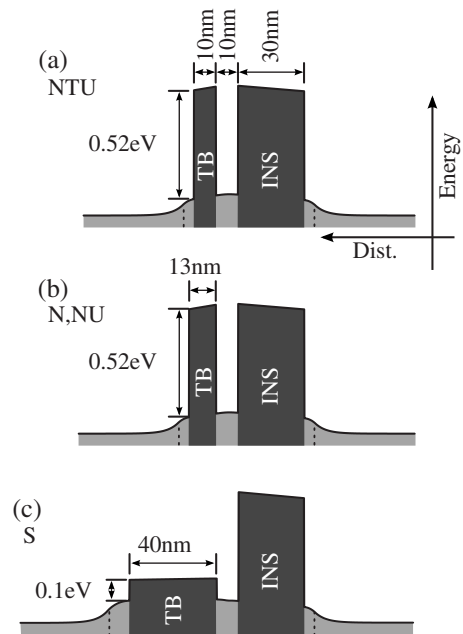

FIG. 4. Schematic band diagrams of the samples used in this experiment. The thickness and alloy composition of the QW and insulating barrier are the same in all samples. (a) Sample NTU. (b) Samples N and NU (they differ only in QW δ doping, which does not significantly affect the diagram on the scale shown here). (c) Sample S. Sample S2 (not shown here) is identical except that the TB is slightly higher (0.13 eV compared to 0.1 eV).

All samples were grown via molecular-beam epitaxy (MBE), lattice matched to n^+ InP substrates. The relevant structure of the samples was nominally identical except for the parameters listed in Table I. In order of growth, the structure was 500 nm n^+ In$_{0.53}$Ga$_{0.47}$As doped 3×10^{18} cm^{-3} with Si; 5 nm undoped In$_{0.53}$Ga$_{0.47}$As; 30 nm In$_{0.53}$Al$_{0.47}$As gate barrier; 10 nm In$_{0.53}$Ga$_{0.47}$As QW (with or without Si δ doping in the center); tunnel barrier of thickness ℓ; undoped In$_{0.53}$Ga$_{0.47}$As spacer layer of thickness w; and 300 nm n^+ In$_{0.53}$Ga$_{0.47}$As doped 3×10^{18} cm^{-3} with Si. Samples S and S2 included an additional, subsequent layer of 50 nm n^+ In$_{0.53}$Ga$_{0.47}$As doped 1×10^{19} cm^{-3} with Si to facilitate making high-conductivity contacts to the top of the structure.

The samples were patterned using conventional photolithographic techniques and were etched into 200 μm diameter mesas. Contacts to the substrate and top of each mesa were formed by sputtering $\sim$10 nm Ti and $\sim$35 nm Au. The mesa sidewall was insulated with $\sim$300 nm SiN deposited by plasma-enhanced chemical vapor deposition. The stray capacitance of the contact to the top of the mesa contributed $\sim$10 pF capacitance in parallel with the device that was constant with frequency to within 50 fF in our measurement range and was therefore easily subtracted from the data. We measured device impedance using an Agilent 4284A *LCR* meter.

IV. EXPERIMENTAL RESULTS: ENERGY DEPENDENCE

The presence of scattering-assisted tunneling can qualitatively alter the energy dependence of tunneling, as illustrated in Eqs. (1) and (2). Here we show how our capacitance measurement of the τ_{rc} enables us to determine this energy dependence, thereby enabling us to determine the dominant transport mechanism in each of our samples.

As discussed in Sec. II, the insulating barrier prevents dc flow and allows μ_{2D} to come into quasiequilibrium with μ_I (although quasiequilibrium is only actually achieved in the absence of V_{ac}). The dc bias V_{dc}, instead of driving a dc current, alters n_S, resulting in direct control over ε_F. Because tunneling in our device occurs predominantly for electrons with energy near μ_{2D}, these electrons have a kinetic energy ε_K in the 2DEG that is approximately equal to ε_F. Thus, our method gives us direct control over ε_K (and parallel momentum $\hbar k_\parallel$) of the tunneling electrons, and this enables us to directly measure the energy dependence of the tunneling by varying V_{dc}.

A. Capacitance-frequency and capacitance-voltage

A representative series of sweeps of capacitance versus frequency at different V_{dc} is shown from sample N in Fig. 5. Two regimes of bias dependence can be seen in panels a and b of Fig. 5. In Fig. 5(a), the principal change is an overall shift to higher frequencies for increasing V_{dc} (and therefore decreasing n_S). In Fig. 5(b), however, V_{dc} becomes large enough to deplete the QW, reducing the low-frequency limit of the capacitance until the QW is fully depleted, at which point the capacitance becomes constant with frequency.

The complementary measurement is shown in Fig. 5(c), where we report the voltage dependence of the capacitance at
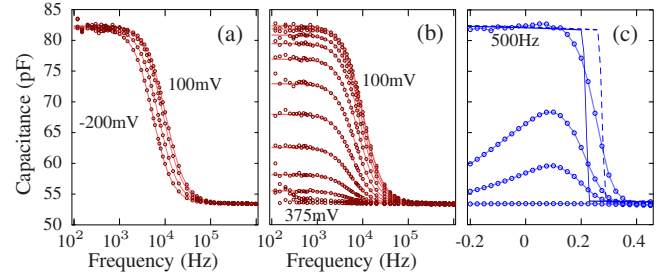

FIG. 5. (Color online) [(a) and (b)] Capacitance-frequency data from sample N taken over a sequence of V_{dc} for T=4.2 K and V_{ac}=5 mV$_{rms}$. Points are data, lines are fits to data using the equivalent circuit of Fig. 2(b). According to our bias convention, n_S decreases with V_{dc}. (a) 100 mV steps in V_{dc}. The QW is occupied in all traces. (b) 25 mV steps in V_{dc}. This range of V_{dc} depletes the QW, reducing the low-frequency limit of the capacitance. (c) Capacitance-voltage data from the same device taken at various values of f (lines with symbols). Also shown are two charge-step simulations of the low-frequency capacitance with different QW δ dopings: 1×10^{11} cm^{-2} (solid line) and 2×10^{11} cm^{-2} (dashed line). The abrupt step of the simulations is not observed in the data because the added impurities make the ground-state energy nonuniform across the sample.

constant frequency. At low frequency (500 Hz), the measured capacitance mimics the energy dependence of the thermodynamic density of states g_{2D} of the 2DEG, which would be a step function in the absence of impurity-induced subband broadening. For comparison, we show simulations of the low-frequency capacitance of the device, which were calculated within a charge-step model[28] using a self-consistent Schrödinger-Poisson solver based on Ref. 29. The only input to these calculations was the expected sample structure; there were no free parameters. Near $V_{dc} \sim 0$ V, electrons have sufficient energy to access the 2DEG, and the capacitance is maximal. As V_{dc} is increased past $\sim$0.25 V, however, ε_0 becomes greater than μ_{2D}. Electrons can therefore no longer access states in the QW, and the capacitance drops.

Also shown in Fig. 5(c) are capacitance-voltage sweeps at higher frequency. The maximal capacitance of these traces is lower than that of the 500 Hz trace because V_{ac} is oscillating too rapidly for electrons to tunnel between the injector and 2DEG to maintain quasiequilibrium between μ_{2D} and μ_I. As can be seen in panels a and b, even 10 kHz is well above the low-frequency regime of the device. For an oscillation frequency f of 1 MHz, there is negligible tunneling because the tunneling rate is orders of magnitude smaller than f, and the capacitance therefore has very little dependence on V_{dc}. (This range of V_{dc} leads to negligible change in the thickness of the depletion region of the 3D regions because of the high doping level; otherwise some decrease in capacitance with V_{dc} would be expected even for high frequencies.)

We expect the behavior of samples S and S2 to be dominated by scattering-assisted tunneling, which should lead to a qualitatively different dependence on V_{dc} in these samples. This is confirmed in the capacitance-frequency sweeps on sample S shown in Fig. 6. In particular, the roll-off frequency abruptly drops by two orders of magnitude for V_{dc} near 210 mV. Also, the capacitance-frequency trace taken in the
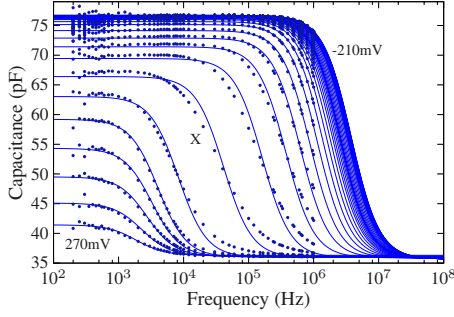
FIG. 6. (Color online) Capacitance versus frequency data from sample S at 5 K, $V_{ac}=5$ mV$_{rms}$, and 10 mV increments of V_{dc}. Points are data, lines are fits using the equivalent circuit model of Figure 2. At $V_{dc}=270$ mV, the QW is almost fully depleted. As V_{dc} is decreased, states in the QW become available, thus increasing the low-frequency capacitance, although the roll-off frequency remains relatively constant. As V_{dc} is decreased near the conditions of trace X ($V_{dc}=210$ mV), the roll-off frequency of the device abruptly increases by two orders of magnitude as a result of the onset of scattering-assisted tunneling. The maximum frequency accessible with our *LCR* meter is 1 MHz.

middle of the transition at $V_{dc}=210$ mV [the trace labeled X in Fig. 6] is not as well described by the equivalent circuit as the traces taken at V_{dc} higher or lower by ∼30 mV. In sample N, in comparison, the equivalent circuit describes the data accurately for all values of V_{dc}. To more quantitatively analyze these effects, we extract the values of τ_{rc} that result from the fits. These are plotted, along with data from samples N, NU, and NTU, in Fig. 7.

B. Quasibound state lifetime versus energy

The values of τ_{rc} in Fig. 7, obtained from fits to the capacitance-frequency curves of Fig. 6, are plotted versus ε_F,
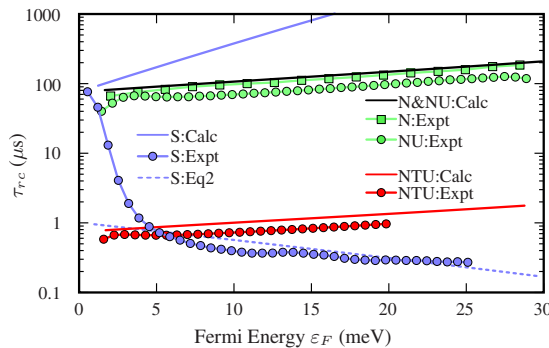

FIG. 7. (Color online) τ_{rc} versus ε_F. Lines with symbols are data; lines without symbols are calculations of scattering-assisted [Eq. (2)] and momentum-conserved (Calc) tunneling. Data from samples N, NU, and NTU all show increasing τ_{rc} with ε_F, in agreement with their respective calculations of momentum-conserved tunneling. (The calculation of NU was nearly identical to that of N and is omitted for clarity.) In contrast, measured τ_{rc} in sample S decreases with ε_F. The calculation including scattering-assisted tunneling [S: Eq. (2)] is a much better description of the data than the calculation of momentum-conserved tunneling (S, Calc). $T=5$ K for sample S; $T=4.2$ K for all others. $V_{ac}=5$mV$_{rms}$.

which was determined for each sample from calibrations of n_S versus V_{dc}, as described in Sec. II. Data from all samples are shown, except for sample S2, which is omitted for clarity. Also plotted are calculations (labeled "Calc") of τ_ℓ for momentum-conserved tunneling that are described in Appendix C. Because there is no applied magnetic field, it is reasonable to assume $g_s \simeq g_{2D}$ (at least at high n_S), and thus we should be able to directly compare these calculations of τ_ℓ with the measured τ_{rc}. These calculations are self-consistent and include effects such as band bending, wave-function penetration into the barriers, and position- and energy-dependent effective masses. Equation (1) provides a simple, intuitive framework through which we can interpret the general features of the data and numerical calculation. While ε_K does not explicitly enter into the description of tunneling in Eq. (1), the calculations of τ_ℓ shown in Fig. 7 increase with ε_F. This is because both ε_0 and, to a lesser extent, the tunnel barrier potential energy ϕ must decrease relative to the potential energy of the injector to accommodate an increase in n_S in order to satisfy the Pauli exclusion principle. The effective barrier height $\phi-\varepsilon_0$ of Eq. (1) therefore has an indirect dependence on ε_F, causing τ_ℓ to increase with ε_F in the calculations. This effect is more pronounced in the calculation of sample S because of its thicker tunnel barrier.

As is evident from Fig. 7, measured τ_{rc} from samples N, NU, and NTU all agree with their respective momentum-conserved calculations of τ_ℓ. This is in agreement with the expected transport behavior of these devices from Fig. 3. In contrast, for sample S the data and the momentum-conserved calculation do not agree. In this sample the measured τ_{rc} actually *decreases* with ε_F, indicating that, in agreement with the predictions of Sec. III, the tunneling in this sample is dominated by scattering-assisted tunneling.

We can use Eq. (2) to predict the energy dependence (that is, the slope of the line in Fig. 7) of the scattering-assisted tunneling lifetime for sample S. (Note that this estimate assumes that the scattering rate ν_S is constant with energy; we will discuss the additional energy dependence of ν_S below.) The slope of this estimate [S: Eq. (2)] is slightly steeper than, but a reasonable approximation of, the slope observed experimentally. The magnitude of the estimate (i.e., the vertical position of the line) is proportional to the scattering time $\tau_s = 1/\nu_S$,

$$\tau_\ell = \alpha \frac{\tau_s}{T_S}, \qquad (9)$$

where α is an unknown proportionality constant. We can estimate what we would expect for τ_s from the Lorentzian half width of the Landau levels[30] (not shown). The half width (Γ) is approximately 3 meV and is approximately independent of field (as in Ref. 30). This yields $\tau_s=\hbar/\Gamma \sim 2 \times 10^{-13}$ s. The other parameter from Eq. (9), α, is unknown, so we simply use it as a fitting parameter. The fit shown in Fig. 7 was achieved for $\alpha=0.005$. To gauge whether this value for α is reasonable, we note that a similar expression for τ_ℓ is true of the momentum-conserved approximation from Eq. (1): $\tau_\ell=\beta/\nu_0 T_0$, where $\nu_0=\varepsilon_0/\hbar$ is the semiclassical tunneling attempt frequency and β is some unknown pro-

portionality constant. Agreement with experiment requires $\beta \sim 0.01$, in approximate agreement with α.

As discussed in Ref. 9, Eq. (2) provides an estimate of the tunneling probability in the asymptotic limit of a very thick barrier. Although the TB in sample S is only 40 nm, this estimate provides a good description of the energy dependence of τ_{rc}, at least over a large range of ε_F. For ε_F near 0 meV, however, τ_{rc} changes abruptly by two orders of magnitude. We believe this change is due to two effects not captured by Eq. (2): the possible formation of a Coulomb gap in the single-particle density of states at low n_S (Ref. 19) and the energy dependence of ν_S.

The formation of a Coulomb gap would increase the ratio g_{2D}/g_s, leading, via Eq. (3), to an increase in τ_{rc}. However, we do not expect the formation of a Coulomb gap to cause g_{2D}/g_s to increase by nearly two orders of magnitude (one order of magnitude or less would be more consistent with previous results[19]). Our results therefore suggest that ν_S has a strong energy dependence near ε_0, regardless of whether a Coulomb gap is formed.

In general, ν_S represents a sum of individual processes such as impurity, alloy, electron-electron, and electron-phonon scatterings. These various scattering mechanisms each depend on quantities such as ε_K or temperature, and thus τ_{rc} will also depend on these quantities in samples dominated by scattering-assisted tunneling. This offers a possible explanation for the abrupt change in τ_{rc} that occurs at low ε_F. For low n_S (and thus low ε_F), the nonuniformities in potential energy that occur across the device become large compared to ε_F (which is simply an average value across the device), and as n_S is further decreased, carriers in the QW can become strongly localized in isolated "pockets" of electrons.[31] Well-width fluctuations of a single monolayer (~ 0.6 nm) have been shown to lead to such localization in thin QWs,[32] and in our system additional potential fluctuations result from the QW δ doping. Once the electrons are strongly localized, the system is said to have undergone a metal-insulator transition.[31,33]

If the electrons are localized to effectively zero-dimensional quantum dots, then the density of states available for scattering will be restricted and scattering will be quenched, leading to a large decrease in the tunneling rate through the barrier. In this case, τ_s should increase greatly as the QW is depleted. As τ_s increases, so should τ_{rc}, but only in devices dominated by scattering-assisted tunneling. Although we can only speculate as to the scale of localization in our devices and whether it is sufficiently small to quench scattering in our devices, we do observe such an abrupt increase as the QW is depleted but only for samples S and S2. These two samples are also the only two we measured in which τ_{rc} decreases with ε_K, the hallmark of transport dominated by scattering-assisted tunneling.

Because this localization will not occur uniformly across the device, we also expect it to alter the line shape of the frequency dependence of the capacitance. As scattering is quenched in some regions of the device and not in others, large variations in τ_{rc} will occur across the device. The characteristic capacitance roll-off that we observe from a single value of τ_{rc} will be broadened by the distribution in τ_{rc}, as is observed for trace X in Fig. 6. This could therefore also explain the poor agreement between this trace and the fit using our equivalent circuit model.

A similar form of localization-induced quenching of scattering occurs in the presence of a perpendicular magnetic field; it is the origin of the quantum Hall effect.[3] As we show in the following section, the samples dominated by scattering-assisted tunneling also display abrupt increases in τ_{rc} at the specific values of V_{dc} and magnetic field at which the integer quantum Hall effect is observed in lateral transport measurements.

V. EXPERIMENTAL RESULTS: MAGNETIC FIELD DEPENDENCE

Our measurements of the energy dependence of scattering-assisted tunneling suggest that localization can quench scattering within the 2DEG and cause τ_{rc} to increase by orders of magnitude. To further probe this possibility, we apply a magnetic field perpendicular to the plane of the 2DEG. This leads to localization effects that are periodic in $1/H$, where H is the applied magnetic field: at integer values of the filling factor $\nu = n_S h/qH$, electrons at the chemical potential are unable to scatter into counter-propagating states because they are trapped in edge states or along local equipotentials. This localization leads to quenching of the scattering within the 2DEG and is the origin of the integer quantum Hall effect.[3]

At even integer ν, the same values at which the integer quantum Hall effect is most readily observed, τ_{rc} increases drastically in samples S and S2, as shown in Fig. 8(a). This effect only occurs in samples that show the zero-field energy dependence characteristic of scattering-assisted tunneling. Because these peaks in τ_{rc} only occur at specific values of H corresponding to even integer ν within the 2DEG, and because they are only present in samples dominated by scattering-assisted tunneling, we believe they result from quenching of the scattering within the 2DEG by the same mechanism that causes the integer quantum Hall effect, magnetic field-induced localization.

As can be seen in Fig. 8(b), all of the samples show similar quantization of g_{2D} into Landau levels. These values of g_{2D} were determined simultaneously with τ_{rc} from fits using the equivalent circuit of Fig. 2 (recall that g_{2D} is proportional to C_Q). The values we measured agree well with previous magnetocapacitance measurements.[16] Additionally, there is quantitative agreement between our results and the model given in Ref. 34. This model represents g_{2D} as a sum of Gaussian Landau levels of rms half width Γ_{LL}. As in Ref. 34, we find best agreement when Γ_{LL} is proportional to $\sqrt{H}$. Our best-fit prefactor of 1.22 meV/T$^{1/2}$ is significantly larger than their (1 meV/T$^{1/2}$), which is consistent with our samples having a significantly lower mobility. The best-fit value of the effective mass is equal to the bulk value of $0.043 m_0$;[35] as expected, the mass enhancement due to nonparabolic bands in the QW is minimal because the wave function extends far into the quaternary barrier where nonparabolicity decreases the effective mass.[36] Because these values of g_{2D} agree quantitatively with both predicted values and previous measurements and were obtained simulta-
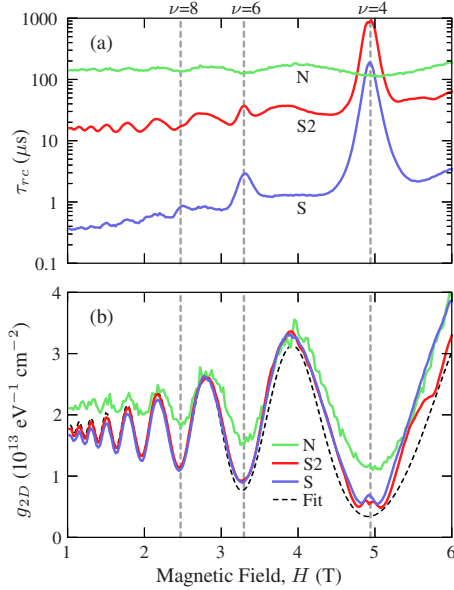
FIG. 8. (Color online) Simultaneous measurements on samples N, S, and S2 of the magnetic field dependence of (a) the quasibound state lifetime (τ_{rc}) and (b) the 2DEG thermodynamic density of states (g_{2D}) at T=1.85 K. V_{dc} was held constant to give $n_S \simeq 4.78 \times 10^{11}$ cm^{-2} in all samples at H=0 T. Values of H corresponding to filling factors ν=4, 6, and 8 are indicated with dotted lines. (a) At ν=4, suppression of the scattering-assisted tunneling increases τ_{rc} by orders of magnitude in samples S and S2. The features at ν=6 and 8 are less pronounced because the Landau-level splitting is smaller at lower H. (b) We also see pronounced dips in g_{2D} at even integer ν, indicating that all three samples show the expected formation of Landau levels. The fit represents the expected behavior of g_{2D} as calculated according to Ref. 34 with a Landau-level half width of Γ_{LL}=(1.22 meV/T$^{1/2}$)$\sqrt{H}$.

neously with τ_{rc} from the fits using the equivalent circuit, we can be confident that the peaks in τ_{rc} in Fig. 8(a) are real variations in τ_{rc} and are not simply the result of errors in fitting or analysis.

In sample N, the measured g_{2D} is slightly noisier than in samples S or S2; this is due to the significantly thinner TB in sample N, which results in a smaller change in capacitance as the QW is depleted. Also, the low-field value of g_{2D} in sample N is slightly larger than in samples S and S2. This difference corresponds to an effective mass that is ~10% larger in sample N, which is due to nonparabolic band enhancement of the effective mass for stronger confinement within the QW. The size of this enhancement is consistent with that observed in cyclotron resonance measurements on similar structures.[37]

There are two small dips in g_{2D} in samples S and S2 adjacent to the minimum at ν=4; these are fitting artifacts that occur because τ_{rc} is varying rapidly, leading to significant variations across the device and poor fits using the equivalent circuit, as in trace X of Fig. 6. The fits (and hence values of g_{2D}) at ν=4 are more accurate because $d\tau_{rc}/dH$ =0 at the local minimum.

We also observed a strong temperature dependence of the peaks in τ_{rc}. Although we have not yet made a thorough investigation of this dependence, we note that for the peak at
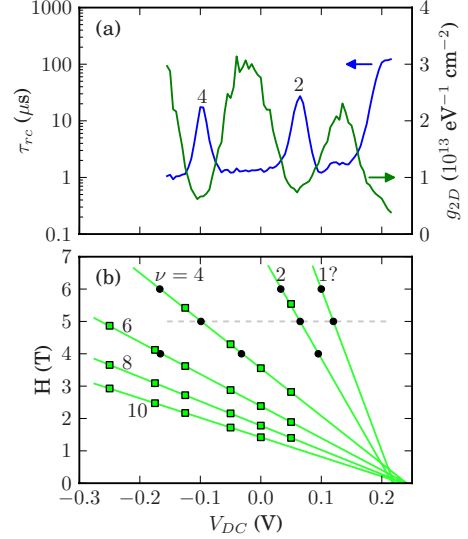

FIG. 9. (Color online) Measurements of sample S in magnetic field versus V_{dc} at T=5 K. (a) τ_{rc} and g_{2D} plotted on the same scales as Fig. 8. The peaks in τ_{rc} are labeled with the corresponding value of ν. Note that these data were acquired at higher temperature than that in Fig. 8. (b) Fan diagram of maxima in τ_{rc} (circles) and minima in magnetocapacitance measurements (squares). Dashed line illustrates the region of the diagram corresponding to the sweep in (a). Solid lines are least-squares fits and are labeled with their corresponding Landau-level filling factor ν. All lines do not intersect at the same value of V_{dc} because the carrier density n_S is not strictly linear with V_{dc} for nonzero H (see Ref. 17 for a thorough discussion of this effect and Ref. 38 for a similar fan diagram).

ν=4 in sample S in Fig. 8(a), τ_{rc} decreased by an order of magnitude as the temperature was raised from 1.85 to 5 K. Values of τ_{rc} adjacent to but off of the peak stayed relatively constant at $\tau_{rc} \simeq 1$ μs.

The data shown in Fig. 8 were taken by sweeping H at a single fixed value of V_{dc}. The complementary measurement, sweeps of V_{dc} at fixed H were also performed, an example of which is shown from sample S at higher temperature (T =5 K) in Fig. 9(a). Note that the peak in τ_{rc} at ν=4 is an order of magnitude smaller than the corresponding in Fig. 8, which was measured at T=1.85 K.

To confirm that the features we observe are correlated with Landau-level filling, we performed several sweeps versus V_{dc} and H. The locations of the peaks in τ_{rc} were recorded in a fan diagram, as shown in Fig. 9. Also shown are the locations of minima in magnetocapacitance traces, which have been shown to be related to minima in the density of states between Landau levels.[38] The slopes of the least-squares fits yield estimates of ν that confirm that the effect we observe occurs at even integer ν. We see an additional smaller peak in τ_{rc} that appears to be related to ν=1, although additional measurements at higher H are needed to make a more accurate characterization of the feature. There is no intrinsic reason that peaks in τ_{rc} should not also appear at odd ν; however, as in the quantum Hall effect, features at odd ν require the electrons to become spin polarized and therefore typically appear at higher H than features at adjacent even values of ν.[3] The onset of these features may be further delayed by the strong disorder in our system.[39]
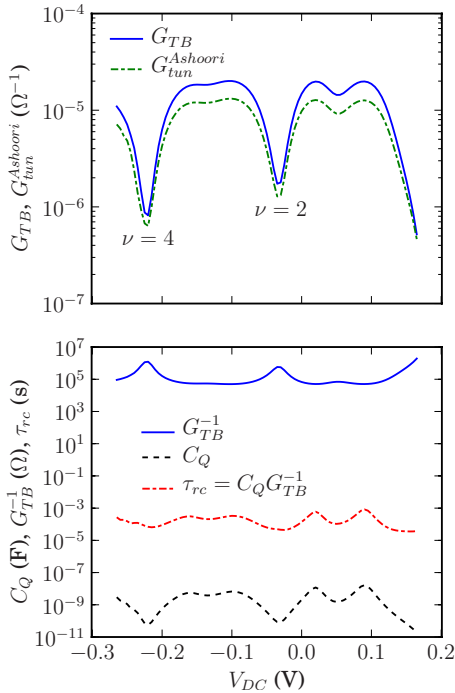
FIG. 10. (Color online) Tunneling conductance calculated by two equivalent models (top panel) and the components of τ_{rc} (bottom panel) plotted versus V_{dc} for sample NU at $H=6$ T and $T=5$ K. The comparison between our analysis technique and that of Ashoori *et al.* (top panel) shows that the two yield almost identical results. The pronounced dips in G_{TB} that occur at $\nu=2$ and 4 reflect dips in g_s. These appear as peaks in the plot of G_{TB}^{-1} (bottom panel). The plot of τ_{rc} nevertheless exhibits dips at $\nu=2$ and 4 because the dips in C_Q at these values of V_{dc} are more pronounced than the peaks in G_{TB}^{-1}.

Few mechanisms other than quenching of the scattering seem adequate to explain the observed peaks in τ_{rc}. The formation of a field-induced Coulomb gap (that is, a decrease in g_s) has been observed in 2D systems such as ours,[18,19,40] and this would modify τ_{rc} via Eq. (3). However, τ_{rc} also depends on g_{2D}, which has been shown to vary much more strongly with Landau-level filling factor ν than does g_s.[18] As a result, the ratio g_{2D}/g_s should vary with ν in a way qualitatively similar to g_{2D}, with possibly a additional slowly varying change due to g_s. We therefore expect that if τ_ℓ were constant, we should observe *dips* in τ_{rc} at even integer ν. This is what is observed in sample N in Fig. 8 as well as in sample NU in Fig. 10. (Incidentally, this validates the analysis of Ashoori *et al.*[18,19] in which τ_ℓ is assumed to be constant.) Such dips are also observed in samples S and S2 in Fig. 8 at low H and in the regions adjacent to even integer ν at higher H. This suggests that the effects of g_{2D} and g_s are similar in all of the samples, as is expected since it is a characteristic of the 2DEG (the characteristics of which are nominally identical in all the samples) and not of the tunnel barrier.

Furthermore, the temperature dependence of g_s has been shown to be independent of ν. In sample S, in contrast, we observed that the peaks in τ_{rc} (which occur at even integer ν) were strong functions of temperature in the range 1.85–5 K, whereas values of τ_{rc} adjacent to but off of the peaks stayed relatively constant.

The scale of resistance change we observe also does not seem consistent with the presence of weak points or defects in the tunnel barrier. Such defects would have a much lower tunneling lifetime than the rest of the QW, leading to significant lateral current spreading within the quantum well that would be suppressed at even integer ν and low n_S. However, it is clear from the frequency dependence of the impedance in sample S at $\nu=4$ (plotted in Appendix B) that the fractional area occupied by weak points is a few percent or less. This implies that the conductivity of the weak spots must be at least four orders of magnitude larger than that of the rest of the barrier to explain the 100-fold increase in conductivity away from integer ν. It seems implausible that such a large variation in tunnel barrier conductivity would occur systematically across multiple devices in high-quality MBE-grown material. Moreover, samples with thin tunnel barriers (N, NU, and NTU), which would seem most prone to growth problems such as dopant diffusion, never exhibited the large spikes in τ_{rc} that were observed in samples S and S2. Furthermore, such highly conducting defects were not observed in the insulating barriers of samples S and S2, and the quaternary barriers in those samples were grown as a digital alloy of ternary layers (1.5 nm superlattice period) in order to avoid any problems specific to the growth of quaternary alloys.

Another aspect of our data that cannot be explained by defects in the tunnel barrier is the dependence of τ_{rc} on n_S in samples S and S2 at zero magnetic field. If our measurement were probing the tunneling resistance of a defect and scattering-assisted tunneling were not a factor, then the tunneling lifetime should increase with n_S as in the control samples, which is not what we observe. On the other hand, it would also be immediately evident if the defect had negligible resistance and we were probing the lateral resistance of the quantum well (i.e., current spreading from the weak point, which would become more conductive with n_S and therefore at first glance might seem to explain our data). In that case the effective/active area of the 2DEG would become frequency dependent, resulting in very poor agreement with our equivalent circuit model, and the measured 2DEG thermodynamic density of states would become strongly dependent on carrier density, which we also do not observe.

We therefore conclude that our samples behave as designed: the control samples (N, NU, and NTU) are dominated by direct tunneling, whereas samples S and S2 are dominated by scattering-assisted tunneling that can be quenched at even integer ν and at low n_S.

VI. OUTLOOK

As we have shown, it is possible to utilize scattering-assisted tunneling as a novel, nonlocal probe of lateral transport within a 2DEG. This opens the door to several new research directions, such as probing the onset of localization in 2DEGs in the form of Wigner crystallization[41] or Anderson localization[31] at low n_S in zero magnetic field, where sample resistance becomes too high for lateral transport measurements. It may also enable the investigation of electron scattering within the interior of quantum spin Hall systems,

which have recently shown edge state transport similar to the quantum Hall effect at zero magnetic field.[42]

At nonzero magnetic field, further measurements are needed to explore the dependence on temperature and carrier density of scattering-assisted tunneling at integer ν. At lower temperatures and higher magnetic fields, it is also possible that this technique could be used to probe the fractional quantum Hall effect. However, proper sample design will be critical because the fractional quantum Hall effect is only observable in high-mobility samples[43] where there is little scattering to cause scattering-assisted tunneling. Also, at lower temperatures it is unclear whether the Coulomb gap[18] will become so large as to be an impediment to our ac measurement technique. However, it is possible that our approach is more sensitive to scattering than lateral transport measurements, which could enable measurements of localization in regimes of mobility and temperature that do not exhibit localization in lateral transport measurements.

Beyond characterization of scattering in 2DEGs, there are other conceivable applications for scattering-assisted tunneling. For example, a device dominated by scattering-assisted tunneling could yield spin-polarized transport if the scattering were spin dependent. The design of the tunnel barrier would greatly enhance the tunneling rate of scattered electrons (as it does in samples S and S2), thereby functioning as a filter for scattered electrons. If carriers of only one spin species were scattered, then the tunnel current would be spin polarized.

In sum, we have directly measured the energy dependence of transport dominated by scattering-assisted tunneling and demonstrated its sensitivity to scattering within a buried 2DEG. By making transport in one direction a function of transport in other directions, scattering-assisted tunneling offers a unique coupling that will undoubtedly find additional applications.

APPENDIX A: DERIVATION OF EQUIVALENT CIRCUIT

There are two popular approaches that can be used to analyze capacitive devices like ours, with the primary difference between the two being the treatment of the capacitance of the 2DEG (which we will call the quantum capacitance C_Q following Ref. 26). In the treatment of Ashoori *et al.*,[19] for example, the device is modeled with an equivalent circuit that does not explicitly include C_Q, and C_Q (or, equivalently, the 2DEG thermodynamic density of states) must be calculated separately. In the analysis of Luyken *et al.*,[24] C_Q is treated explicitly. While the two methods of analysis are ultimately equivalent, it is important to not confuse the two

approaches. For example, the lifetime $\tau_{rc}=R_{TB}C_Q$ that we extract from our equivalent circuit is not able to be described using the equivalent circuit of Ashoori *et al.* because that circuit does not include C_Q.

Both approaches begin with an equation [Eq. (1) in Ref. 24 or Eq. (A4) in Ref. 19] describing the tunneling current between the injector and the 2DEG,

$$\frac{d\sigma_{2D}}{dt} = \frac{1}{\tau_\ell} q g_s \Delta\mu, \tag{A1}$$

where $\sigma_{2D} = q n_S$ is the charge density in the QW, τ_ℓ is the quasibound state lifetime of the QW, g_s is the 2DEG single-particle density of states (which governs the tunneling rate), and $\Delta\mu = \mu_I - \mu_{2D}$ is the chemical potential difference between the injector and 2DEG.

We calculate the electrostatic response of the device, following the analysis of Luyken *et al.*, as

$$q g_{2D} \Delta\mu = -\Delta\sigma_{2D} + q^2 g_{2D} \Delta\phi, \tag{A2}$$

where $\Delta\sigma_{2D}$ is the net difference between σ_{2D} and its time-averaged value; and $\Delta\phi$ is the change in electrostatic potential between the injector and QW, which accounts for both the effects of electron charging in the QW and the applied bias $V_{ac}=V_0 e^{i\omega t}$. Note that the thermodynamic DOS g_{2D} is the relevant quantity here. Without loss of generality, we can define s such that $s=g_s/g_{2D}$. Multiplying both sides of Eq. (A2) by s and plugging into Eq. (A1), we arrive at

$$\frac{d\sigma_{2D}}{dt} = \frac{d\Delta\sigma_{2D}}{dt} = -\frac{s}{\tau_\ell}\left(\Delta\sigma_{2D} - \frac{C_Q}{A}\Delta\phi\right), \tag{A3}$$

where $C_Q = q^2 g_{2D} A$ for device area A.

The difference between the electric fields in the tunnel barrier and insulating barrier is proportional to the sheet charge of the 2DEG, which allows us to find $\Delta\phi$,

$$\Delta\phi = \frac{C_G}{C_{TB}+C_G} V_0 e^{i\omega t} - \frac{A}{C_{TB}+C_G}\Delta\sigma_{2D}, \tag{A4}$$

where C_{TB} and C_G are the geometric capacitances of the tunnel barrier and insulating barrier, respectively. Defining $\tau_{rc}=\tau_\ell/s$, we arrive at the nonhomogeneous differential equation

$$\frac{d\Delta\sigma_{2D}}{dt} + \frac{1}{\tau_{rc}}\left(1 + \frac{C_Q}{C_{TB}+C_G}\right)\Delta\sigma_{2D}$$

$$= \frac{1}{\tau_{rc}}\frac{C_G C_Q}{C_{TB}+C_G}\frac{V_0}{A}e^{i\omega t}, \tag{A5}$$

which has the solution

$$\Delta\sigma_{2D} = \frac{V_0}{A}e^{i\omega t}\frac{C_G C_Q^*}{C_{TB}+C_G+C_Q^*}, \tag{A6}$$

where $C_Q^* = C_Q/(1+i\omega\tau_{rc})$. Using Eq. (A4), it is trivial to find $\Delta\sigma_I$, the charge density change on the injector,

$$\Delta\sigma_I = \frac{C_{TB}}{A}\Delta\phi = \frac{C_{TB}}{C_Q^*}\Delta\sigma_{2D}. \qquad (A7)$$

Note that in the limit $\tau_{rc} \to 0$ this relation reduces to $\Delta\sigma_I / \Delta\sigma_{2D} = C_{TB}/C_Q$, consistent with the calculation of Luryi.[26]

We thus arrive at the equation determining the current response of the device,

$$I(t) = A\frac{d}{dt}(\Delta\sigma_{2D} + \Delta\sigma_I) = i\omega V_0 e^{i\omega t} C_G \frac{C_{TB} + C_Q^*}{C_{TB} + C_G + C_Q^*},$$

$$(A8)$$

which is equivalent to that of the circuit shown in Fig. 2, provided that $R_{TB} = \tau_{rc}/C_Q$.

In Fig. 10(a), we compare this analysis with that of Ashoori *et al.*[18,19] in which they use a different equivalent circuit (but equivalent overall analysis) to find the tunneling conductance $G_{tun}^{Ashoori} = q^2 A g_s / \tau_\ell$. By our analysis, this is given by $G_{TB} = C_Q / \tau_{rc}$. It is apparent from the close agreement of the two traces that these two analyses are equivalent.

Figure 10(b) provides a visual description of why we observe dips in τ_{rc} at even integer ν in samples with momentum-conserved tunneling. Essentially this is because g_{2D} varies more strongly with ν than does g_s.

APPENDIX B: FITTING

The fitting of the complex impedance using the equivalent circuit of Fig. 2(b) was done using the least-square function of the mathematical software package OCTAVE. We obtained identical results using the Fortran library MINPACK from within the statistical software package R. C_G was held fixed at an estimated, bias-dependent value during fitting. Using Eq. (A8), we fit the impedance of the device using C_Q and $\tau_{rc} = R_{TB}C_Q$ as free parameters rather than C_Q and R_{TB} independently. The 95% confidence interval of the fit parameters was typically less than 10% of their value. Error in estimated C_G leads to additional uncertainty in τ_{rc} ($\sim 10\%$) but such error results in a systematic shift in τ_{rc} and does not significantly affect our analysis.

Example fits from samples N and S are shown in Fig. 11. It is evident that the equivalent circuit provides an accurate description of device behavior in both cases. Figure 11(a) shows sample N (a control sample) under conditions of zero magnetic field and zero applied bias. In Figs. 11(b) and 11(c), data are shown from sample S over a range of ν including $\nu = 2$. At $\nu = 2$, lateral transport within the 2DEG is suppressed, quenching scattering. These conditions also serve to isolate any conductive defects in the barrier, preventing current fan-out from the defect within the QW. Thus, if a significant area of the tunnel barrier were defective, it would be manifested as a significant broadening of the frequency dependence in Figs. 11(b) and 11(c). Although the fits are not perfect, they are closer than would be possible if even a few percent of the area of the tunnel barrier were defective. The slight broadening that is observed (relative to the fit to the equivalent circuit) is not surprising; any areas of the sample in which scattering has not been fully quenched
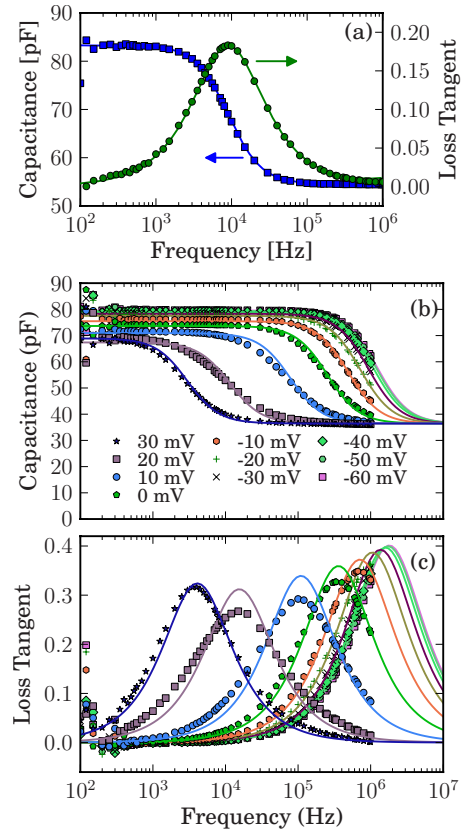

FIG. 11. (Color online) Measured capacitance and loss tangent versus frequency (symbols) and fits to both components of the data simultaneously using the equivalent circuit of Fig. 2(b) (lines). (a) Sample N measured at $H=0$ T, $V_{dc}=0$ V, and $T=4.2$ K. [(b) and (c)] Sample S measured at a variety of V_{dc} with $T=5$ K and $H=6$ T. The bias $V_{dc}=30$ mV corresponds to $\nu=2$; $V_{dc}=-60$ mV corresponds to midway between $\nu=2$ and 4.

at 6 T will tunnel with a faster rate. Supporting this interpretation is the observation that the quality of the fit at $\nu=2$ continually improves as H is increased to 6 T, the maximum field attainable in our system, and we therefore expect that the quality of the fit would be even better at higher magnetic fields. Also, because of the large QW impurity concentration in this sample, the Landau levels are not fully formed, g_{2D} is still measurably large at $\nu=2$, and thus even at $\nu=2$ there is a capacitance step at low f. Over the plotted range of V_{dc}, g_{2D} changes by slightly more than a factor of 6.

APPENDIX C: CALCULATION OF τ_ℓ IN THE ABSENCE OF SCATTERING

We can compare our measured values of τ_{rc} with theoretical estimates of τ_ℓ, which we calculate in the absence of scattering using the energy width Γ of the quasibound state resonance. First we found the self-consistent potential-energy profile of our device using a conventional Schrödinger-Poisson solver based on Ref. 29. This calculation finds the quasiequilibrium distribution of charge across the device, accounting for such effects as conduction-band bowing within the QW and wave-function penetration into

the barriers. Using the equilibrated conduction-band profile, we then solved the Schrödinger equation for the entire device (including the 3D conducting contacts, which enter as self-energies) using a nonequilibrium Green's-function (NEGF) formalism within a single-band effective-mass model. Generally we followed the treatment of Refs. [11] and [44]. It should be noted that the plane-wave eigenstate basis was used for the transverse directions and no transitions between states of different $k_\parallel$ were allowed, thereby ensuring momentum is conserved in the plane of the QW.[45] (We did not use the NEGF formalism to find the self-consistent conduction-band profile because the width of our quasibound state resonance is so small that the calculation would have had to been performed at a prohibitively large number of energies.) The NEGF calculation determined the spectral function $A(z, z', \varepsilon_z)$ of the device, where ε_z is the energy associated with motion in the z direction. The diagonal elements of A (elements for which $z = z'$) are proportional to the density matrix of the system.[44] For energies near the quasibound state resonance, the energy dependence of $A(z, z, \varepsilon_z)$ for z in the center of the QW can be approximated with a Lorentzian function,

$$A(z_{QW}, z_{QW}, \varepsilon_z) = \frac{\alpha}{(\varepsilon_z - \varepsilon_0)^2 + (\Gamma/2)^2}, \qquad (C1)$$

where ε_0 is the energy of the center of the resonance, Γ is its characteristic width, α is a proportionality constant, and $z = z_{QW}$ in the center of the QW.[44] We extract Γ from the calculation of A by fitting A with the function in Eq. (C1). Typical values for Γ were of order 10^{-11} eV. The tunneling rate $1/\tau_\ell$ is related to the width of the quasibound state resonance by $1/\tau_\ell = \Gamma/h$,[46] which allows us to easily find τ_ℓ.

Adding scattering to this calculation is not trivial because once the quasibound state is "dressed" by scattering interactions, it will in general no longer have a Lorentzian energy profile,[47] and $\tau_\ell = h/\Gamma$ will no longer hold. Well-developed methods[11,44,45] of calculating transport in the presence of scattering typically treat only steady-state transport, which is negligible in our devices. Although fully quantum mechanical calculations of scattering-assisted transport in our device are clearly needed, they are outside the scope of our experiment.

---

*venky@seas.harvard.edu

†Present address: Materials Department, University of Delaware, Newark, DE.

[1] L. Chang, L. Esaki, and R. Tsu, Appl. Phys. Lett. **24**, 593 (1974).

[2] J. Faist, F. Capasso, D. Sivco, C. Sirtori, A. Hutchinson, and A. Cho, Science **264**, 553 (1994).

[3] D. Yoshioka, *The Quantum Hall Effect* (Springer-Verlag, Berlin, Germany, 2002).

[4] Z. A. Weinberg, J. Appl. Phys. **53**, 5052 (1982).

[5] E. E. Mendez, E. Calleja, and W. I. Wang, Phys. Rev. B **34**, 6026(R) (1986).

[6] P. M. Solomon, S. L. Wright, and C. Lanza, Superlattices Microstruct. **2**, 521 (1986).

[7] P. Guéret, C. Rossel, W. Schlup, and H. P. Meier, J. Appl. Phys. **66**, 4312 (1989).

[8] J. A. Lebens, R. H. Silsbee, and S. L. Wright, Appl. Phys. Lett. **51**, 840 (1987).

[9] S. V. Meshkov, Sov. Phys. JETP **64**, 1337 (1986).

[10] F. Chevoir and B. Vinter, Phys. Rev. B **47**, 7260 (1993).

[11] R. Lake, G. Klimeck, R. C. Bowen, and D. Jovanovic, J. Appl. Phys. **81**, 7845 (1997).

[12] R. M. Feenstra, D. A. Collins, D. Z.-Y. Ting, M. W. Wang, and T. C. McGill, Phys. Rev. Lett. **72**, 2749 (1994).

[13] If the scattering is elastic, $k_\parallel$ must be restored after tunneling, and this restricts the scattering to second-order or higher processes; see Ref. [9].

[14] M. Kaplit and J. N. Zemel, Phys. Rev. Lett. **21**, 212 (1968).

[15] A. Voshchenkov and J. Zemel, Phys. Rev. B **9**, 4410 (1974).

[16] T. P. Smith, B. B. Goldberg, P. J. Stiles, and M. Heiblum, Phys. Rev. B **32**, 2696 (1985).

[17] O. E. Dial, R. Ashoori, L. Pfeiffer, and K. West, Nature (London) **448**, 176 (2007).

[18] R. C. Ashoori, J. A. Lebens, N. P. Bigelow, and R. H. Silsbee, Phys. Rev. Lett. **64**, 681 (1990).

[19] R. C. Ashoori, J. A. Lebens, N. P. Bigelow, and R. H. Silsbee, Phys. Rev. B **48**, 4616 (1993).

[20] V. T. Dolgopolov, A. A. Shashkin, A. V. Aristov, D. Schmerek, W. Hansen, J. P. Kotthaus, and M. Holland, Phys. Rev. Lett. **79**, 729 (1997).

[21] R. Ashoori and R. Silsbee, Solid State Commun. **81**, 821 (1992).

[22] R. C. Ashoori, H. L. Stormer, J. S. Weiner, L. N. Pfeiffer, S. J. Pearton, K. W. Baldwin, and K. W. West, Phys. Rev. Lett. **68**, 3088 (1992).

[23] G. Medeiros-Ribeiro, J. M. Garcia, and P. M. Petroff, Phys. Rev. B **56**, 3609 (1997).

[24] R. J. Luyken, A. Lorke, A. O. Govorov, J. P. Kotthaus, G. Medeiros-Ribeiro, and P. M. Petroff, Appl. Phys. Lett. **74**, 2486 (1999).

[25] J. Brews, Solid-State Electron. **21**, 345 (1978).

[26] S. Luryi, Appl. Phys. Lett. **52**, 501 (1988).

[27] Z. A. Weinberg, Solid-State Electron. **20**, 11 (1977).

[28] V. Temple and J. Shewchun, IEEE Trans. Electron Devices **18**, 235 (1971).

[29] I.-H. Tan, G. L. Snider, L. D. Chang, and E. L. Hu, J. Appl. Phys. **68**, 4071 (1990).

[30] R. Ashoori, Ph.D. dissertation, Cornell University, 1992.

[31] T. Ando, A. B. Fowler, and F. Stern, Rev. Mod. Phys. **54**, 437 (1982).

[32] A. Zrenner, L. V. Butov, M. Hagn, G. Abstreiter, G. Böhm, and G. Weimann, Phys. Rev. Lett. **72**, 3382 (1994).

[33] E. Ribeiro, R. D. Jäggi, T. Heinzel, K. Ensslin, G. Medeiros-Ribeiro, and P. M. Petroff, Phys. Rev. Lett. **82**, 996 (1999).

[34] J. P. Eisenstein, H. L. Stormer, V. Narayanamurti, A. Y. Cho, A. C. Gossard, and C. W. Tu, Phys. Rev. Lett. **55**, 875 (1985).

[35] I. Vurgaftman, J. R. Meyer, and L. R. Ram-Mohan, J. Appl.

Phys. **89**, 5815 (2001).

[36] D. F. Nelson, R. C. Miller, and D. A. Kleinman, Phys. Rev. B **35**, 7770 (1987).

[37] C. Wetzel, R. Winkler, M. Drechsler, B. K. Meyer, U. Rössler, J. Scriba, J. P. Kotthaus, V. Härle, and F. Scholz, Phys. Rev. B **53**, 1038 (1996).

[38] T. W. Hickmott, Phys. Rev. B **32**, 6531 (1985).

[39] D. R. Leadley, R. J. Nicholas, J. J. Harris, and C. T. Foxon, Phys. Rev. B **58**, 13036 (1998).

[40] J. P. Eisenstein, L. N. Pfeiffer, and K. W. West, Phys. Rev. Lett. **69**, 3804 (1992).

[41] A. V. Filinov, M. Bonitz, and Y. E. Lozovik, Phys. Rev. Lett. **86**, 3851 (2001).

[42] A. Roth, C. Brune, H. Buhmann, L. W. Molenkamp, J. Maciejko, X. Qi, and S. Zhang, Science **325**, 294 (2009).

[43] A. M. Chang, M. A. Paalanen, D. C. Tsui, H. L. Störmer, and J. C. M. Hwang, Phys. Rev. B **28**, 6133 (1983).

[44] S. Datta, *Electronic Transport in Mesoscopic Systems* (Cambridge University Press, Cambridge, UK, 1995).

[45] S. Datta, Superlattices Microstruct. **28**, 253 (2000).

[46] E. Merzbacher, *Quantum Mechanics*, 3rd ed. (Wiley, New York, 1998).

[47] R. Lake, G. Klimeck, R. C. Bowen, C. Fernando, T. Moise, Y. C. Kao, and M. Leng, Superlattices Microstruct. **20**, 279 (1996).